

Suzaku Spectroscopy of the Extended X-Ray Emission in M17

Yoshiaki HYODO,¹ Masahiro TSUJIMOTO,^{2,3,4} Kenji HAMAGUCHI,^{5,6} Katsuji KOYAMA,¹
Shunji KITAMOTO,² Yoshitomo MAEDA,⁷ Yohko TSUBOI⁸, and Yuichiro EZOE⁹

¹*Department of Physics, Graduate School of Science, Kyoto University,
Kita-shirakawa Oiwake-cho, Sakyo, Kyoto 606-8502*

²*Department of Physics, Rikkyo University, 3-34-1 Nishi-Ikebukuro, Toshima, Tokyo 171-8501*

³*Department of Astronomy & Astrophysics, Pennsylvania State University,
525 Davey Laboratory, University Park, PA 16802, USA*

⁴*Chandra Fellow*

⁵*CRESST and X-ray Astrophysics Laboratory, Goddard Space Flight Center,
National Aeronautics and Space Science, Greenbelt, MD 20771, USA*

⁶*Universities Space Research Association, 10211 Wincopin Circle, Suite 500, Columbia, MD 21044, USA*

⁷*Institute of Space and Astronautical Science, Japan Aerospace Exploration Agency,
3-1-1 Yoshinodai, Sagami, Kanagawa 229-8510*

⁸*Department of Science and Engineering, Chuo University, 1-13-27 Kasuga, Bunkyo, Tokyo 112-8551*

⁹*Cosmic Radiation Laboratory, RIKEN, 2-1 Hirosawa, Wako, Saitama 351-0198
hyodo@cr.scphys.kyoto-u.ac.jp*

(Received ; accepted)

Abstract

We present the results of a Suzaku spectroscopic study of the soft extended X-ray emission in the H II region M17. The spectrum of the extended emission was obtained with a high signal-to-noise ratio in a spatially-resolved manner using the X-ray Imaging Spectrometer (XIS). We established that the contamination by unresolved point sources, the Galactic Ridge X-ray emission, the cosmic X-ray background, and the local hot bubble emission is negligible in the background-subtracted XIS spectrum of the diffuse emission. Half a dozen of emission lines were resolved clearly for the first time, including $K\alpha$ lines of highly ionized O, Ne, and Mg as well as L series complex of Fe at 0.5–1.5 keV. Based on the diagnosis of these lines, we obtained the following results: (1) the extended emission is an optically-thin thermal plasma represented well by a single temperature of $\sim 3.0 \pm 0.4$ MK, (2) the abundances of elements with emission lines in the diffuse spectrum are 0.1–0.3 solar, while those of bright discrete sources are 0.3–1.5 solar, (3) the metal abundances relative to each other in the diffuse emission are consistent with solar except for a Ne enhancement of a factor of ~ 2 , (4) both the plasma temperature and the chemical composition of the diffuse emission show no spatial variation across the studied spatial scale of ~ 5 pc.

Key words: X-rays: ISM — ISM: bubbles — ISM: H II regions — Galaxy: open clusters and associations: individual (M17)

1. Introduction

Massive stars are a driving force of physical and chemical evolutions of their host galaxies. Supernova explosions and their remnants have been intensively studied for decades, but the pre-explosion effects are equally important; the integrated mass, momentum, and energy releases over the lifetime of an O star can be comparable to those by a supernova explosion at the end of their lives (Leitherer et al. 1992). Diffuse X-ray emission is generated as a consequence of shocks by stellar winds impinging on the interstellar medium (ISM). Therefore, we can quantitatively study the effects of energy dissipation and the chemical enrichment of interstellar space by early-type stars through the spectroscopy of X-ray emission in H II regions.

Weaver et al. (1977) presented a self-similar solution of stellar winds interacting with the ISM. They showed a sin-

gle O7 star forms a hot ($\sim 10^{6-7}$ K) bubble by the shock, which can be observed as soft extended (~ 10 pc) X-ray emission. Townsley et al. (2003) claimed the first unambiguous detections of such emission in the H II regions M17 and the Rosette Nebula using the Advanced CCD Imaging Spectrometer (ACIS; Garmire et al. 2003) onboard the Chandra X-ray Observatory (Weisskopf et al. 2002). With a ~ 40 ks integration time of M17 (ObsID = 972), diffuse soft X-ray emission was detected apart from 886 point sources above $\sim 10^{29.3}$ erg s⁻¹ (Broos et al. 2007). Dunne et al. (2003) showed the entire structure of the soft X-ray diffuse emission using the Position-Sensitive Proportional Counter (PSPC; Pfeffermann et al. 1987) onboard ROSAT (Trümper 1982). They measured the total X-ray luminosity and compared to the wind-blown bubble models with and without heat conduction. They concluded that only the bubble without heat conduction can account for the observed X-ray luminosity of $\sim 2.5 \times 10^{33}$ erg s⁻¹. The

magnetic field may be responsible for suppressing the heat conduction and mass evaporation between the hot gas and cold ISM (Dunne et al. 2003).

The results obtained by these high-resolution imaging studies are generally consistent with the wind-blown bubble models. However, the observational results are not still accurate enough to compare to the theoretical works. It is often ambiguous whether the observed diffuse emission is from wind-blown bubbles or from supernovae, which give rise to diffuse emission with a similar X-ray spectral hardness and luminosity in a similar spatial scale. The largest uncertainty stems from the lack of spectral analysis based on line diagnostics in a spatially-resolved manner.

Resolving emission lines is crucial to examine whether the spectrum is thermal and to determine the temperature and the chemical composition of the plasma. For example, the intensity ratio of $K\alpha$ lines between O VII and O VIII and that between Ne IX and Ne X are steep functions of the plasma temperature at 1–10 MK (Tucker & Gould 1966). In between the O and Ne $K\alpha$ complex, Fe L series lines dominate the spectrum. The metallicity of these elements is one of the factors to determine the X-ray luminosity expected from a wind-blown bubble (Chu et al. 1995). The anomaly in the O and Fe abundance ratio can be used to discriminate different types of supernovae (Tsujimoto et al. 1995; Nomoto et al. 1997) if the emission is of a supernova origin. The previous studies using ROSAT and Chandra were incapable of resolving these lines, limiting their ability to diagnose the plasma emission.

The X-ray Imaging Spectrometer (XIS; Koyama et al. 2007) onboard Suzaku (Mitsuda et al. 2007) has a superior spectral resolution, a low background, and a large effective area, which are particularly suited for spectroscopy of extended X-ray emission. The capability to resolve key elements with sufficient statistical significance has been illustrated by several initial studies on extended emission in H II regions (Hamaguchi et al. 2007; Tsujimoto et al. 2007). Hamaguchi et al. (2007) resolved various emission lines from the diffuse emission in the Carina Nebula. Based on the low nitrogen-to-oxygen ratio and the spatial variation of the Fe and Si abundances, they suggested that the diffuse emission originates not from wind-blown bubbles but from one or multiple old supernova remnant(s).

M17 is a Galactic H II region at a distance of ~ 1.6 kpc (Nielbock et al. 2001). Hanson et al. (1997) identified nine O stars in the central OB association with near infrared spectroscopy. A much larger number of young OB stars are suggested by near infrared photometry (Lada et al. 1991; Jiang et al. 2002). The earliest system is a binary of two O4–O5 stars. The age of the cluster is estimated to be $\lesssim 1$ Myr based on the H-R diagram (Hanson et al. 1997). Strong winds and radiation from the central OB association sculpted the ambient matter to form a V-shaped cloud, which was traced by molecular and atomic hydrogen lines (Chrysostomou et al. 1992; Felli et al. 1984; Brogan & Troland 2001). The diffuse X-ray emission found by Chandra and ROSAT has an asymmetric morphology with respect to the OB association and

fills the cavity of the molecular cloud toward the negative Galactic latitude (Povich et al. 2007).

M17 is suitable for X-ray studies of hot bubbles in H II regions for being proximate and having a very high contrast of the diffuse emission against point sources. From the Chandra study (Townsend et al. 2003), the diffuse emission is more intense than the integrated emission of resolved point sources by more than ten-fold at 1 keV. Despite the limited spatial resolution of Suzaku, therefore, the obtained spectrum is not seriously contaminated by unresolved point sources.

2. Observation

Suzaku observed M17 on 2006 March 11–14 in the first announcement of opportunity observing cycle. Suzaku has XIS and Hard X-ray Detector (HXD; Kokubun et al. 2007; Takahashi et al. 2007) instruments. We concentrate on the XIS data in this paper, which has a sensitivity for the soft emission studied here.

The XIS is equipped with four X-ray CCDs. Three of them (XIS0, 2, and 3) are front-illuminated (FI) CCDs and the remaining one (XIS1) is a back-illuminated (BI) CCD. Each CCD chip has a format of 1024×1024 pixels and is composed of four segments of 256×1024 pixels. FI and BI CCDs are superior to each other in the hard and soft band responses, respectively. They are mounted at the focus of four independent X-ray telescopes (XRT; Serlemitsos et al. 2007). The detectors are sensitive in the energy range of 0.2–12.0 keV with an initial energy resolution of ~ 65 eV in the full width at half maximum and a total effective area of ~ 1360 cm² at 1.5 keV. An XIS field of view covers a $\sim 18' \times 18'$ region with a half power diameter of $\sim 2'$. The radioactive sources of ⁵⁵Fe illuminate two corners of each of the four CCDs for calibration purposes.

The performance of XIS is subject to degradation due to the radiation damage in the orbit (Koyama et al. 2007). As of the observation date, the energy resolution in the full width at half maximum is ~ 90 eV at 1.5 keV. The relative energy gains among XIS chips and segments have a systematic uncertainty of ~ 5 eV. An unknown contaminant accumulates on the optical blocking filters of the XIS in the orbit. As a result, the effective area at the soft band end has diminished significantly, making the carbon and nitrogen features difficult to detect below ~ 0.5 keV. This effect is included in the auxiliary response.

The observation was conducted using the normal clocking mode with a frame time of 8 s. Data (revision 1.2¹) were screened to remove events during the South Atlantic Anomaly passages, at elevation angles below 4° from the earth rim, and at elevation angles below 10° from sunlit earth rim. We constructed plots of the raw count rate versus the elevation angles to find that these criteria maximize the exposure time with negligible contaminating emission. After the filtering, the net integration time is ~ 110 ks.

¹ See <http://www.astro.isas.jaxa.jp/suzaku/process/> for details.

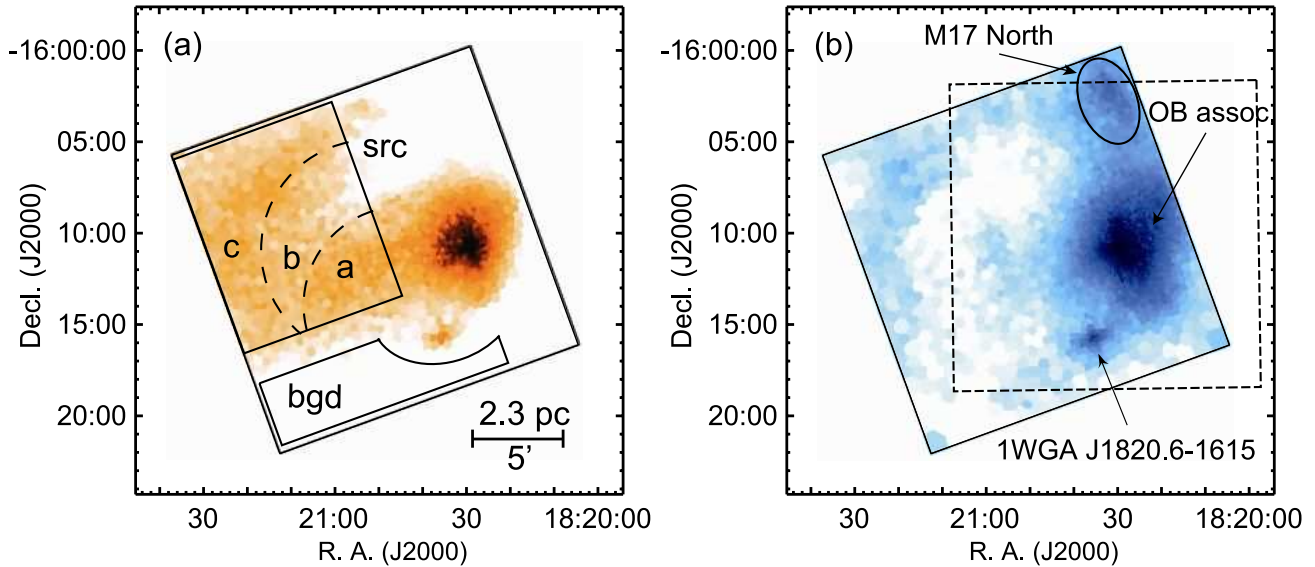


Fig. 1. XIS images in the (a) 0.5–1.5 keV and (b) 1.5–5 keV bands. The XIS field is shown with the solid square in both panels, while the ACIS field is shown with the dashed square in (b). The source and background regions for diffuse emission are shown by solid lines in (a). The source sub-regions (a, b, and c) are ruled by dashed curves. The discrete sources are shown with arrows in (b). Both images are processed as follows: (1) Non-X-ray background constructed from night earth observations was subtracted. (2) The astrometry and vignetting were corrected. (3) The images were adaptively binned to achieve a signal-to-noise ratio of larger than 8 using the weighted Voronoi tessellation algorithm (Diehl et al. 2006, Cappellari et al. 2003).

3. Analysis

3.1. Image Analysis

Figure 1 shows the XIS images of the study field in the (a) soft (0.5–1.5 keV) and (b) hard (1.5–5.0 keV) bands. The two band-limited images appear strikingly different. In the hard band, the image is dominated by the emission from the OB association. We also see the excess emission from a group of protostars M17 North (Wilson et al. 1979; Henning et al. 1998; Broos et al. 2007). In the soft band, the extended emission emerges in the eastward of the OB association, as was claimed by Townsley et al. (2003) and Dunne et al. (2003). The XIS observation was centered at the most intense part of the extended emission at (R.A., decl.) $\sim (18^{\text{h}}20^{\text{m}}50^{\text{s}}, -16^{\circ}12')$ in the equinox J2000.0, while the ACIS observation was at the OB association (Townsley et al. 2003). The XIS and ACIS images have a similar size (~ 18 and ~ 17 arc-minute square, respectively) with a $\sim 70\%$ overlapping area (figure 1b).

The astrometry of the XIS frame was registered using 1WGA J1820.6–01615 found in both images. The O8 star (Ogura & Ishida 1976; White et al. 1994) is bright, isolated, and point-like in the ACIS image (CXOU J182035.87–161542.5; Broos et al. 2007), thus serves as a good astrometric calibrator. We shifted the XIS frame by $\sim 17''$ to the north so that the position matches with that by the ACIS observation. The Chandra frame is accurate to $\sim 0''.5$ in the astrometry².

² See <http://cxc.harvard.edu/proposer/POG> for details.

3.2. Spectral Analysis of Extended Emission

3.2.1. Entire Emission

We first examine the spectrum of the entire diffuse emission. We extracted the source spectrum from a rectangular region and the background spectrum from a region devoid of intense diffuse emission (figure 1a). Because the off-axis angles of the source and background regions are different, we processed the raw spectra in the following way before subtracting the background from the source: (1) The non-X-ray-background (NXB) spectrum was subtracted, which was constructed from night earth data at the same extraction region. The NXB of XIS is a function of the geomagnetic cut-off rigidity. We therefore compiled night earth observations such that the cut-off rigidity distribution becomes the same with that of the M17 observation. (2) The vignetting was corrected by multiplying the effective area ratios between the source and background regions for each energy bin of the background spectrum. This takes into account the accumulating contaminant on the XIS optical blocking filter.

The merged FI and the BI spectra are shown in figure 2. In the merged FI spectrum, we added the three FI spectra to increase the photon statistics, because the redistribution matrix functions (RMFs) and the auxiliary response functions (ARFs) are essentially the same for these chips. On the other hand, we handled the BI spectrum separately for its different response.

We resolved the emission lines clearly for the first time, which include K shell lines of O, Ne, and Mg as well as L shell lines of Fe. This indicates that the emission is of a thermal origin. The O VIII line is much stronger than the O VII line and the Ne IX line is so than the Ne X line

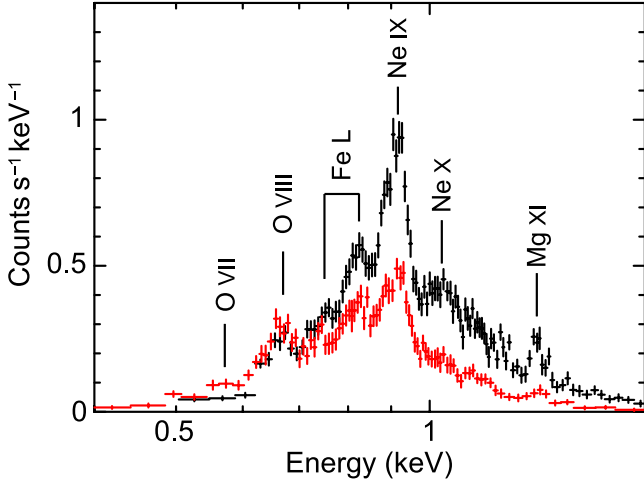


Fig. 2. Background-subtracted XIS spectra of the entire diffuse emission (regions a+b+c in figure 1a). BI spectrum is shown in red, while the merged FI spectrum is in black in a linear scale. Conspicuous emission lines are labeled, which are $K\alpha$ lines except for the Fe L series lines.

if we taking the energy dependence of the efficiencies into account. These line ratios alone infer that the plasma temperature is in the range of 2.5–4 MK (Tucker & Gould 1966) even without spectral model fittings.

3.2.2. Spatially-Resolved Emission

In order to investigate the spatial difference of the plasma properties, we divided the source region into three sub-regions (a, b, and c in figure 1a) based on the morphology of the diffuse emission. We constructed the spectra from each region and subtracted the background in the same manner for the entire emission. The merged FI and the BI spectra in each sub-region are shown in figure 3.

We fitted the 0.4–1.8 keV spectra with a thin-thermal plasma model at a collisional equilibrium (the APEC model; Smith et al. 2001) convolved with the interstellar absorption (Morrison & McCammon 1983). The abundances of the noticeable elements (O, Ne, Mg, and Fe) were free parameters. Those of the other elements were fixed at 0.3 solar, which is canonically used in X-ray spectroscopy in star-forming regions (e.g., Getman et al. 2005). We used the RMFs (version 2006-08-01) of the observation month and generated ARFs using a ray-tracing simulator (`xissimarfgen` version 2006-08-28; Ishisaki et al. 2007) assuming that the emission is uniform across a 15' radius circle centered at the optical axis. In order to compensate for the possible uncertainty in the energy gain calibration, we introduced an additional fitting parameter (offset). The resultant offset values were 1–4 eV, which are within the current calibration limitation.

A single temperature model yielded acceptable fits for all spectra. The best-fit hydrogen-equivalent column density (N_H), plasma temperature ($k_B T$), metallicity (Z_O , Z_{Ne} , Z_{Mg} , and Z_{Fe}), the average surface brightness (S_X), and the luminosity (L_X) in the 0.5–2.0 keV band are summarized in table 1. The best-fit models are shown in figure 3. We attempted different plasma models with mul-

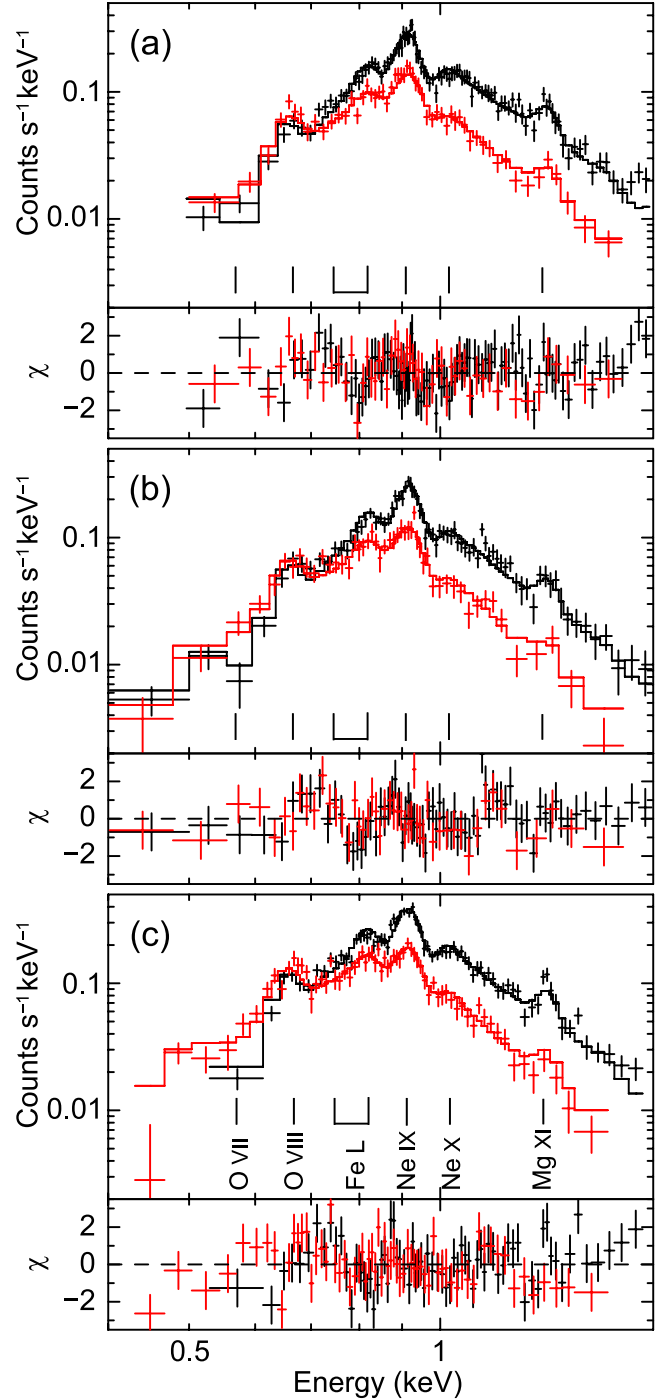


Fig. 3. Background-subtracted 0.4–1.8 keV band spectra of the diffuse emission in the three regions (a), (b), and (c) in figure 1 (a). The BI spectrum is shown in red, while the merged FI spectrum is in black in a logarithmic scale. The upper panels show the data in crosses and the best-fit models in solid lines, while the lower panels show residuals to the fit.

multiple temperatures or non-equilibrium ionization, but did not obtain improved fits. We therefore consider that a single temperature model at a collisional equilibrium is adequate.

3.3. Spectral Analysis of Discrete Sources

We also constructed spectra of the three discrete sources (1WGA J1820.6–1615, M17 North, and the OB association in figure 1b). The source signals were accumulated from elliptical regions of $2'0$ – $3'5$ axis lengths, while the background signals were from adjacent regions free of sources. The spectra are shown in figure 4. All the spectra are characterized by hard emission full of $K\alpha$ emission lines of highly ionized ions, which include Mg XI, Mg XII, Si XIII, Si XIV, S XV, S XVI, Ar XVII, Ar XVIII, Ca XIX, and Fe XXV.

We can have a crude estimate for spectral models from the intensity of these lines. The spectra of 1WGA J1820.6–1615 and the OB association show a Mg XI line stronger than Mg XII as well as Fe XXV and a hard continuum up to ~ 8 keV, requiring at least two thermal components of different temperatures. M17 North shows a Mg XII line and no prominent Mg XI line, thus a single temperature model would be adequate.

We fitted these spectra using the attenuated thin-thermal plasma model similarly for the diffuse emission. The merged FI and the BI spectra were simultaneously fitted for 1WGA J1820.6–1615 and the OB association. Only the merged FI spectrum was fitted for the M17 North because its BI spectrum is strongly contaminated by the ^{55}Fe calibration source. We first fitted the spectra with a one-temperature model. An additional component with a different temperature was added if the fitting was rejected due to systematic residuals. As the crude estimate, the spectra of 1WGA J1820.6–1615 and the OB association required a two-temperature model, while that of the M17 North was fitted by a one-temperature model. The best-fit models and parameters are shown in figure 4 and table 2, respectively.

4. Discussion

4.1. Contamination to the Extended Emission

The spectra of the diffuse emission in figures 2 and 3 are contaminated by other sources of emission. We evaluate the levels of contamination by unresolved point sources, the Galactic Ridge X-ray emission (GRXE), the cosmic X-ray background (CXB), and the local hot bubble (LHB), and argue that their contributions to the background-subtracted spectra are negligible. About 70% of the XIS field is covered in the Chandra observation (figure 1b), which has a much better spatial resolution and sensitivity for faint point sources (Townsend et al. 2003; Broos et al. 2007). Among the three sub-regions, the region (a) has a complete coverage by Chandra. We therefore use this sub-region as a representative to evaluation the levels of various contaminations.

First, we examine the contribution of unresolved point sources. We extracted 19 point sources from the ACIS

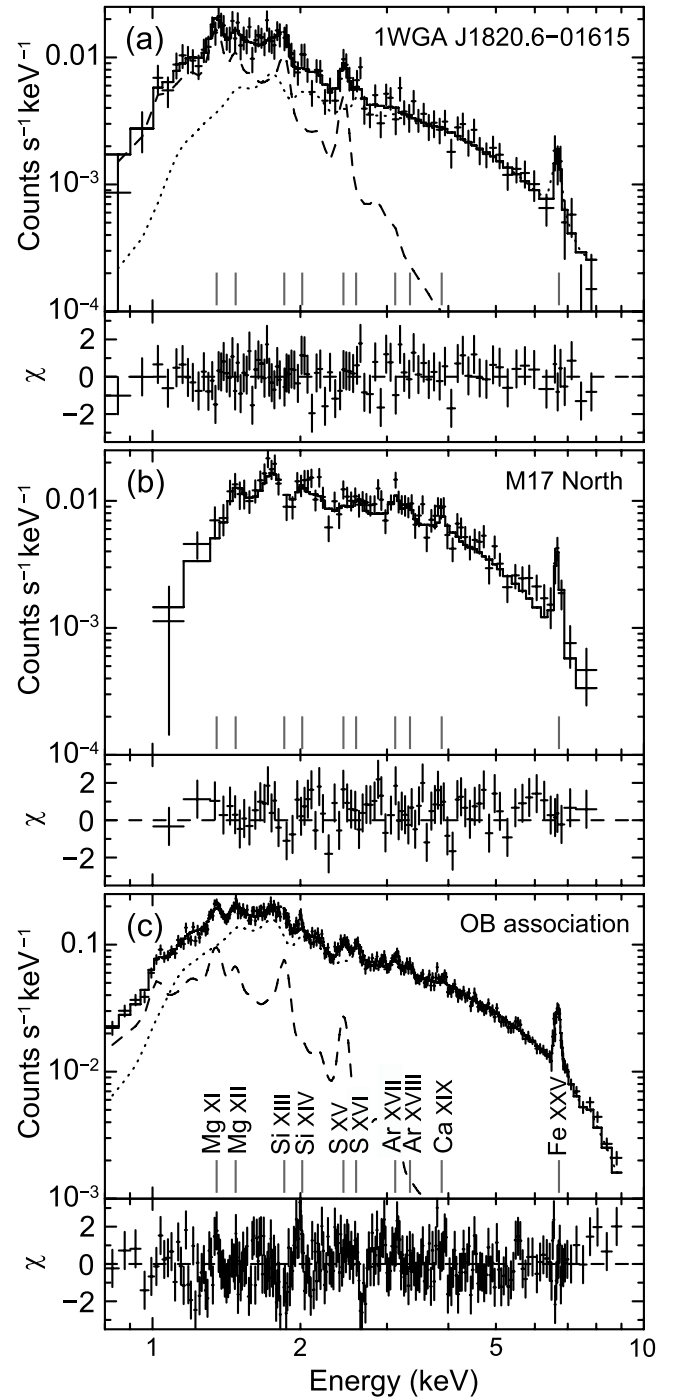


Fig. 4. Background-subtracted 0.8–10 keV band spectra of the three discrete sources: (a) 1WGA J1820.6–1615, (b) M17 North, and (c) the OB association. The symbols follow figure 3. The higher and lower temperature components of the two temperature model are shown respectively with dashed and dotted lines. For simplicity, only the merged FI spectra and the best-fit models are shown.

Table 1. Best-fit APEC parameters for the spatially-resolved diffuse spectra.

Pars.	Units	Sub-regions		
		(a)	(b)	(c)
N_{H}^*	(10^{21} cm $^{-2}$)	4.8 (4.4–5.2)	4.6 (4.4–5.2)	4.3 (3.7–4.6)
$k_{\text{B}}T^*$	(keV)	0.25 (0.24–0.27)	0.24 (0.22–0.25)	0.27 (0.25–0.28)
Z_{O}^*	(solar)	0.10 (0.06–0.14)	0.15 (0.11–0.18)	0.13 (0.10–0.16)
Z_{Ne}^*	(solar)	0.20 (0.17–0.24)	0.32 (0.25–0.39)	0.22 (0.19–0.26)
Z_{Mg}^*	(solar)	0.10 (0.09–0.13)	0.12 (0.07–0.16)	0.12 (0.09–0.16)
Z_{Fe}^*	(solar)	0.10 (0.08–0.13)	0.19 (0.14–0.20)	0.12 (0.11–0.14)
$S_{\text{X}}^{*\dagger}$	(10^{-14} erg s $^{-1}$ cm $^{-2}$ arcmin $^{-2}$)	2.16 (2.12–2.21)	1.34 (1.31–1.38)	1.55 (1.52–1.58)
L_{X}^{\ddagger}	(10^{33} erg s $^{-1}$)	1.3	1.0	1.2
$\chi^2/\text{d.o.f}$		155.5/146	121.8/114	176.9/129

* The uncertainties in the parentheses are the 90% confidence range.

† The average X-ray surface brightness in the 0.5–2.0 keV band.

‡ The absorption-corrected X-ray luminosity in the 0.5–2.0 keV band. A distance of 1.6 kpc is assumed.

Table 2. Best-fit APEC parameters for the discrete spectra.

Pars.	Units	1WGA J1820.6–01615	M17 North	OB association
N_{H}^*	(10^{22} cm $^{-2}$)	1.7 (1.4–2.0)	2.4 (2.1–2.7)	1.3 (1.2–1.4)
$k_{\text{B}}T_{\text{high}}^{*\dagger}$	(keV)	3.8 (3.1–4.7)	2.7 (2.4–3.2)	4.0 (3.9–4.1)
$k_{\text{B}}T_{\text{low}}^{*\dagger}$	(keV)	0.56 (0.47–0.65)	...	0.59 (0.56–0.62)
Z_{Ne}^*	(solar)	0.3	0.3	0.51 (0.34–0.71)
Z_{Mg}^*	(solar)	0.49 (0.24–0.87)	0.3	0.51 (0.38–0.65)
Z_{Si}^*	(solar)	0.30 (0.16–0.58)	0.3	0.53 (0.39–0.71)
Z_{S}^*	(solar)	1.07 (0.58–1.72)	0.3	1.17 (0.98–1.38)
Z_{Ar}^*	(solar)	0.3	1.67 (0.72–3.00)	1.44 (1.00–1.90)
Z_{Ca}^*	(solar)	0.3	0.3	0.46 (0.01–0.90)
Z_{Fe}^*	(solar)	0.33 (0.19–0.48)	0.36 (0.22–0.50)	0.28 (0.25–0.31)
$F_{\text{X}}^{*\ddagger}$	(10^{-13} erg s $^{-1}$ cm $^{-2}$)	3.9 (3.8–4.0)	7.4 (7.1–7.7)	58.3 (57.8–58.8)
L_{X}^{\S}	(10^{32} erg s $^{-1}$)	3.2	4.9	30.0
$\chi^2/\text{d.o.f}$		100.2/134	66.4/76	473.3/405

* The uncertainties in the parentheses are the 90% confidence range. Fixed values are shown without ranges.

† The plasma temperatures for the higher and lower temperature components. Only the higher temperature value is given for M17 North, which is fitted by a single temperature model.

‡ The X-ray flux in the 1.0–8.0 keV band.

§ The absorption-corrected X-ray luminosity in the 1.0–8.0 keV band. A distance of 1.6 kpc is assumed.

data in the sub-region (a), constructed the composite spectrum, and fitted it with a thermal plasma model. The spectrum of each source is too poor to fit individually, so we assume that all sources have the same spectral shape that best describes the composite spectrum. Using their positions, flux, and the assumed spectral shape, we generated their XIS events using a ray-tracing simulator (`xissim`; Ishisaki et al. 2007). In figure 5, we compare the integral of the simulated spectra of unresolved point sources (PS1) to the observed diffuse spectrum (pluses). In the displayed observed spectrum, we subtracted the NXB spectrum but not the background spectrum in the neighboring region. The point source contribution accounts for $\sim 8\%$ of the emission in the 0.4–1.8 keV band.

To have an estimate of the maximum contamination to the lines, we repeated the same procedure using the model with the maximum allowable abundance values in the best-fit model for simulating unresolved point source events. The resultant integrated spectrum (PS2) is also shown in figure 5. At the Ne IX line at 0.92 keV, the

contribution by the point sources accounts only for $<10\%$ of the observed emission.

Second, we derive the GRXE contribution, which is ubiquitous along the Galactic Plane at Galactic longitudes (l) of $|l| \lesssim 45^\circ$ (Kaneda et al. 1997; Sugizaki et al. 2001). We refer to a Chandra result (Ebisawa et al. 2005) for the spectral shape in the soft band and to a Rossi X-ray Timing Explorer result (Revnivtsev et al. 2006) for the surface brightness at the position of M17 ($l \sim 15^\circ$). The GRXE contribution to the observed emission is estimated to be $\sim 3\%$ and is shown in figure 5.

Third, for the CXB contribution, we consulted the Suzaku XIS observation of the North Ecliptic Pole (Fujimoto et al. 2007) both for the spectral shape and the surface brightness. The CXB was observed and fitted by a power-law model. We convolved the model with the XIS responses and found that the contribution is $\sim 2\%$.

Finally, we constrain the contribution by the LHB emission. We estimate its surface brightness to be $\sim 4 \times 10^4$ counts s $^{-1}$ arcmin $^{-2}$ in the PSPC R1 and

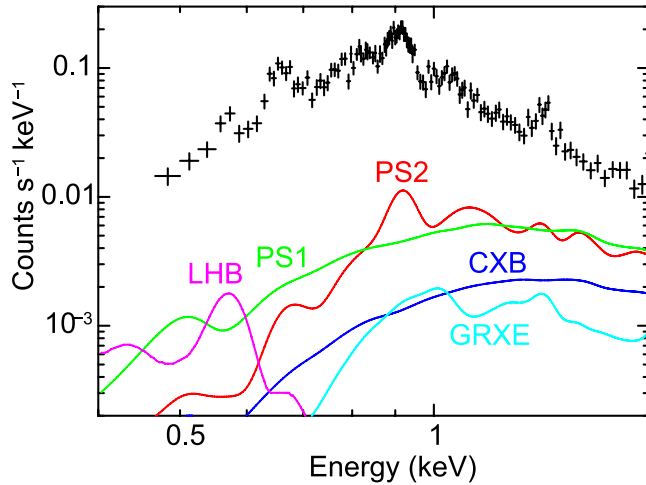


Fig. 5. Comparison of the observed diffuse spectrum to the simulated spectra of contaminating sources. The NXB signal is subtracted from the observed spectrum. PS1 and PS2 are for the contribution of unresolved point sources with different spectral models, GRXE for the Galactic Ridge X-ray emission, CXB for the cosmic X-ray background, and LHB for the local hot bubble. None of them play a significant contribution. Moreover, most of them are removed by subtracting a background spectrum from the neighboring region.

R2 bands (Snowden et al. 1998). We assume that the spectrum is a thin-thermal plasma (the Raymond-Smith model; Raymond & Smith 1977) with a temperature of 0.1 keV. With the derived emission measure of $\sim 2.8 \times 10^{-3} \text{ cm}^{-6} \text{ pc}$, the LHB contributes $\sim 2\%$ of the observed emission.

None of the above components play a significant role in the observed diffuse spectrum. Moreover, we removed most of them by subtracting a background spectrum from a neighboring region. The background events show no indication of time variability caused by solar flares (Fujimoto et al. 2007). We conclude that the background-subtracted XIS spectrum represents the spectrum of the uncontaminated diffuse emission quite well.

The background spectrum accounts for $\sim 35\%$ of the source spectrum of the sub-region (a). Besides the NXB contributing $\sim 7\%$ of the source flux, the sum of unresolved point sources, GRXE, CXB, and LHB contributes $\sim 15\%$. Therefore, emission with a flux of $\sim 13\%$ of the source flux is additionally included in the background spectrum. The contribution from the bright sources outside of the extraction region is negligible. We attribute the remaining emission to the diffuse emission in the background region (figure 1a). If this is the case, the flux estimate of the diffuse emission (table 1) is underestimated by $\sim 13\%$.

4.2. Comparison with Previous Studies

We compare our results with the previous works using ROSAT (Dunne et al. 2003) and Chandra (Townsend et al. 2003; Broos et al. 2007). We derived that the diffuse spectrum is explained by an absorbed single temperature thin-thermal plasma model of $k_B T \sim 0.25 \text{ keV}$ and $N_H \sim 4.5 \times 10^{21} \text{ cm}^{-2}$. The total luminosity (0.5–2.0 keV)

in the combined (a)+(b)+(c) region is $\sim 3.5 \times 10^{33} \text{ erg s}^{-1}$ (table 1).

The ROSAT study (Dunne et al. 2003) shows that the total luminosity of the diffuse emission is $\sim 2.5 \times 10^{33} \text{ erg s}^{-1}$. The smaller estimate than our result is more noticeable if we consider that the ROSAT value was derived from a larger area and in a wider energy range (0.1–2.4 keV). This stems from an underestimate of the extinction. Without a sufficient spectral resolution to resolve lines, two different models were not disentangled in the ROSAT PSPC spectra; one is a low plasma temperature with a large extinction ($\sim 0.2 \text{ keV}$ and $\sim 10^{22} \text{ cm}^{-2}$) and the other is a high plasma temperature with a small extinction ($\sim 0.7 \text{ keV}$ and $\sim 10^{20} - 10^{21} \text{ cm}^{-2}$). Dunne et al. (2003) derived the luminosity based on the latter, but our spectroscopy shows that the former should be in the case.

The best-fit XIS values of L_X and N_H are consistent with those presented in the Chandra study (Townsend et al. 2003), in which $L_X = 3.4 \times 10^{33} \text{ erg s}^{-1}$ (0.5–2.0 keV), and $N_H = (4 \pm 1) \times 10^{21} \text{ cm}^{-2}$. However, the plasma temperatures are different between the two studies. In Chandra, the primary component of $k_B T = 0.6 \pm 0.1 \text{ keV}$ and the secondary component of $\sim 0.13 \text{ keV}$ were claimed. In Suzaku, however, we confirmed that a single temperature component of $\sim 0.25 \text{ keV}$ is adequate from the diagnosis of resolved oxygen and neon lines.

From the discrete sources, we detected $K\alpha$ emission lines from highly ionized ions (figure 4). The spectrum of the OB association is comprised of hundreds of point sources, but the emission from an O4–O5 binary dominates the spectrum. Broos et al. (2007) claimed that both components of the binary (sources 543 and 536) have plasma temperatures exceeding 10 keV. However, the strong Fe XXV $K\alpha$ line at 6.7 keV and the weak Fe XXVI $K\alpha$ line at 7.0 keV in the XIS spectrum (figure 4c) do not support such high temperatures.

4.3. Spatial Difference of the Plasma Properties

A high signal-to-noise ratio spectrum by XIS enabled us to conduct spatially-resolved spectroscopy of the diffuse emission. The plasma temperature and the chemical composition are uniform, except possibly for a larger metallicity in the sub-region (b). The Chandra study (Townsend et al. 2003) also show no evidence for spatial variation of plasma temperature.

The observed uniformity indicates that the entire plasma is at a thermal equilibrium in the observed spatial scale of $\sim 5 \text{ pc}$, unless the plasma is patchy at equilibria locally by magnetic confinement. The global equilibrium is reasonable considering the fact that the plasma sound crossing time ($\sim 2 \times 10^4 \text{ yr}$) is much smaller than the time scale of the system ($\sim 10^6 \text{ yr}$), thus the constant pressure is achieved (Weaver et al. 1977). Here, we used the plasma volume and the electron density as $\sim 30 \text{ pc}^3$ and $\sim 1 \text{ cm}^{-3}$, respectively, by assuming that the plasma distribution has a conical shape with its apex at the OB association and with a filling factor of 1. Given the uniformity of the plasma temperature and pressure, we speculate that the

density is also spatially uniform.

The observed surface brightness, however, is different among the three sub-regions (figure 1a, table 1). It is ~ 1.6 times more intense in the sub-region (a) than (b). This is not attributable entirely to the different extinction, as N_{H} is larger in the sub-region (a) than in (b). Because the plasma has a uniform temperature and density, we speculate that the difference of the surface brightness is likely due to the different line-of-sight depths or different filling factors.

With the derived plasma volume and the density, the total mass of the plasma is $\sim 1 M_{\odot}$. This is comparable to the integrated ejecta mass by stellar winds at a mass loss rate of $\sim 10^{-6} M_{\odot}$ for $\sim 10^6$ yr and agrees with the estimates by the previous works (Dunne et al. 2003; Townsley et al. 2003). We also speculate that the swept-up and evaporated ISM does not make a significant contribution to the plasma mass.

4.4. Chemical Composition

The chemical composition of the diffuse emission is revealed for the first time in this study. The metallicity of the diffuse emission is 0.1–0.3 solar (table 1), which is significantly lower than those derived for the discrete sources (0.3–1.5 solar). The metal abundances relative to each other in the diffuse emission are consistent with solar among O, Mg, and Fe (Anders, Grevesse 1989), but Ne is enhanced in all three sub-regions by a factor of ~ 2 (table 1). This is also evident in the simultaneous spectral fits of the three sub-regions, in which we tied the abundance values of these elements. The resultant values are $Z_{\text{O}} = 0.12$ (0.11–0.13), $Z_{\text{Ne}} = 0.22$ (0.21–0.25), $Z_{\text{Mg}} = 0.10$ (0.08–0.12), and $Z_{\text{Fe}} = 0.12$ (0.11–0.13) solar.

Such Ne enhancement from other metals is widely seen in coronally active stars (Brinkman et al. 2001; Kastner et al. 2002; Audard et al. 2003; Imanishi et al. 2003; Stelzer & Schmitt 2004; Maggio et al. 2007) for unknown reasons. We consider that the Ne enhancement is an intrinsic feature of the diffuse plasma, and is not influenced by the contamination of Ne-enhanced point sources spectra (§ 4.1). One explanation for the anomaly is that the poorly-constrained solar Ne abundance is underestimated by a factor of a few (Drake & Testa 2005; Liefke & Schmitt 2006). This would account for the observed Ne enhancement in the M17 diffuse plasma as well.

The lack of a clear spatial variation of the chemical composition comprises a sharp contrast to the diffuse emission in the Carina Nebula (Hamaguchi et al. 2007), where the different abundance patterns across a similar spatial scale suggest the supernova origin for the emission. In the diffuse emission in M17, the O and Fe ratio is consistent with the solar abundance, which is another line of evidence against the supernova interpretation. If a supernova has occurred in M17, it should have been caused by a star earlier than the earliest (O4–O5) star in the OB association. Such a massive source causes a core-collapse-type supernova. It would have yielded a measurably larger ratio of O against Fe than the solar value by a factor of a few (Tsujiimoto et al. 1995; Nomoto et al. 1997).

5. Summary

We conducted a spectroscopic study of the soft diffuse X-ray emission in M17 using the XIS onboard Suzaku. High signal-to-noise ratio spectra of the diffuse emission were obtained in a spatially-resolved manner. Half a dozen of emission lines were resolved clearly for the first time, which include $K\alpha$ lines from highly ionized O, Ne, and Mg and L lines from Fe. These lines are clear evidence for the thermal origin of the diffuse emission.

Based on the Chandra data of an overlapping field and on the previous works in the literature, we confirmed that the background-subtracted diffuse spectrum by XIS is barely contaminated by unresolved point sources, GRXE, CXB, and LHB emission.

We showed that the diffuse spectra are explained by a single temperature plasma model of $k_{\text{B}}T \sim 0.25$ keV, $L_{\text{X}} \sim 3.5 \times 10^{33}$ erg s $^{-1}$ (0.5–2.0 keV), and $N_{\text{H}} \sim 4.5 \times 10^{21}$ cm $^{-2}$. The temperature and the chemical composition of the diffuse plasma is spatially uniform, indicating that the plasma is at a thermal equilibrium. The apparent difference in the surface brightness is probably due to the difference in the line-of-sight depth or in the filling factors, and not in the plasma density.

The abundance is obtained individually for the detected elements, which are consistent with 0.1–0.3 solar values. The enhancement of Ne against other metals by a factor of ~ 2 is seen in the diffuse plasma, which may be explained by an upward revision of the solar Ne abundance.

The lack of spatial variations in the chemical composition comprises a sharp contrast to the diffuse emission in the Carina Nebula, where different abundance patterns across a similar spatial scale suggest the supernova origin for the emission. Together with the O to Fe ratio consistent with the solar value, this gives evidence against the interpretation that a supernova is the cause of the diffuse emission observed in M17.

The authors thank Takashi Hosokawa for useful discussion. Y. H. and M. T. acknowledge financial support from the Japan Society for the Promotion of Science. The work is supported by the Grants-in-Aid for the 21st century center of excellence program “Center for Diversity and Universality in Physics” and for the program number 18204015 from the Ministry of Education, Culture, Sports, Science and Technology of Japan. The research made use of data obtained from the Data ARchive and Transmission System (DARTS), provided by the PLAIN center, ISAS/JAXA.

References

- Anders, E., & Grevesse, N. 1989, *Geochim. Cosmochim. Acta*, 53, 197
- Audard, M., Güdel, M., Sres, A., Raassen, A. J. J., & Mewe, R. 2003, *A&A*, 398, 1137
- Brinkman, A. C., et al. 2001, *A&A*, 365, L324
- Brogan, C. L., & Troland, T. H. 2001, *ApJ*, 560, 821
- Broos, P. S., Feigelson, E. D., Townsley, L. K., Getman, K. V., Wang, J., Garmire, G. P., Jiang, Z., & Tsuboi, Y. 2007,

- ApJS, 169, 353
- Cappellari, M., & Copin, Y. 2003, MNRAS, 342, 345
- Chrysostomou, A., Brand, P. W. J. L., Burton, M. G., & Moorhouse, A. 1992, MNRAS, 256, 528
- Chu, Y.-H., Chang, H.-W., Su, Y.-L., & Mac Low, M.-M. 1995, ApJ, 450, 157
- Diehl, S., & Statler, T. S. 2006, MNRAS, 368, 497
- Drake, J. J., & Testa, P. 2005, Nature, 436, 525
- Dunne, B. C., Chu, Y.-H., Chen, C.-H. R., Lowry, J. D., Townsley, L., Gruendl, R. A., Guerrero, M. A., & Rosado, M. 2003, ApJ, 590, 306
- Ebisawa, K., et al. 2005, ApJ, 635, 214
- Felli, M., Massi, M., & Churchwell, E. 1984, A&A, 136, 53
- Fujimoto, R., et al. 2007, PASJ, 59, S133
- Garmire, G. P., Bautz, M. W., Ford, P. G., Nousek, J. A., & Ricker, G. R., Jr. 2003, Proc. SPIE, 4851, 28
- Getman, K. V., et al. 2005, ApJS, 160, 319
- Hamaguchi, K., et al. 2007, PASJ, 59, S151
- Hanson, M. M., Howarth, I. D., & Conti, P. S. 1997, ApJ, 489, 698
- Henning, T., Klein, R., Launhardt, R., Lemke, D., & Pfau, W. 1998, A&A, 332, 1035
- Imanishi, K., Nakajima, H., Tsujimoto, M., Koyama, K., & Tsuboi, Y. 2003, PASJ, 55, 653
- Ishisaki, Y., et al. 2007, PASJ, 59, S113
- Jiang, Z., et al. 2002, ApJ, 577, 245
- Kaneda, H., Makishima, K., Yamauchi, S., Koyama, K., Matsuzaki, K., & Yamasaki, N. Y. 1997, ApJ, 491, 638
- Kastner, J. H., Huenemoerder, D. P., Schulz, N. S., Canizares, C. R., & Weintraub, D. A. 2002, ApJ, 567, 434
- Kokubun, M., et al. 2007, PASJ, 59, S53
- Koyama, K., et al. 2007, PASJ, 59, S23
- Lada, C. J., Depoy, D. L., Merrill, K. M., & Gatley, I. 1991, ApJ, 374, 533
- Leitherer, C., Robert, C., & Drissen, L. 1992, ApJ, 401, 596
- Liefke, C., & Schmitt, J. H. M. M. 2006, A&A, 458, L1
- Maggio, A., Flaccomio, E., Favata, F., Micela, G., Sciortino, S., Feigelson, E. D., & Getman, K. V. 2007, ApJ, 660, 1462
- Mitsuda, K., et al. 2007, PASJ, 59, S1
- Morrison, R., & McCammon, D. 1983, ApJ, 270, 119
- Nielbock, M., Chini, R., Jütte, M., & Manthey, E. 2001, A&A, 377, 273
- Nomoto, K., Hashimoto, M., Tsujimoto, T., Thielemann, F.-K., Kishimoto, N., Kubo, Y., & Nakasato, N. 1997, Nuclear Physics A, 616, 79
- Ogura, K., & Ishida, K. 1976, PASJ, 28, 35
- Pfeffermann, E., et al. 1987, Proc. SPIE, 733, 519
- Povich, M. S., et al. 2007, ApJ, 660, 346
- Raymond, J. C., & Smith, B. W. 1977, ApJS, 35, 419
- Revnivtsev, M., Molkov, S., & Sazonov, S. 2006, MNRAS, 373, L11
- Serlemitsos, P. J., et al. 2007, PASJ, 59, S9
- Smith, R. K., Brickhouse, N. S., Liedahl, D. A., & Raymond, J. C. 2001, ApJL, 556, L91
- Snowden, S. L., Egger, R., Finkbeiner, D. P., Freyberg, M. J., & Plucinsky, P. P. 1998, ApJ, 493, 715
- Stelzer, B., & Schmitt, J. H. M. M. 2004, A&A, 418, 687
- Sugizaki, M., Mitsuda, K., Kaneda, H., Matsuzaki, K., Yamauchi, S., & Koyama, K. 2001, ApJS, 134, 77
- Takahashi, T., et al. 2007, PASJ, 59, S35
- Townsley, L. K., Feigelson, E. D., Montmerle, T., Broos, P. S., Chu, Y.-H., & Garmire, G. P. 2003, ApJ, 593, 874
- Trümper, J. 1982, Advances in Space Research, 2, 241
- Tsujimoto, T., Nomoto, K., Yoshii, Y., Hashimoto, M., Yanagida, S., & Thielemann, F.-K. 1995, MNRAS, 277, 945
- Tsujimoto, M., Hyodo, Y., & Koyama, K. 2007, PASJ, 59, S229
- Tucker, W. H., & Gould, R. J. 1966, ApJ, 144, 244
- Weaver, R., McCray, R., Castor, J., Shapiro, P., & Moore, R. 1977, ApJ, 218, 377
- Weisskopf, M. C., Brinkman, B., Canizares, C., Garmire, G., Murray, S., & van Speybroeck, L. P. 2002, PASP, 114, 1
- White, N. E., Giommi, P., & Angelini, L. 1994, IAU Circ., 6100, 1
- Wilson, T. L., Fazio, G. G., Jaffe, D., Kleinmann, D., Wright, E. L., & Low, F. J. 1979, A&A, 76, 86